(Preprint) AAS 20-575

OBSERVABILITY METRICS FOR SPACE-BASED CISLUNAR DOMAIN AWARENESS

Erin E. Fowler[*], Stella B. Hurtt[†], and Derek A. Paley[‡]

We present a dynamic simulation of the cislunar environment for use in numerical analysis of various pairings of resident space objects and sensing satellites intended for cislunar space domain awareness (SDA). This paper's contributions include analysis of orbit families for the mission of space-based cislunar domain awareness and a set of metrics that can be used to inform the specific orbit parameterization for cislunar SDA constellation design. Additionally, by calculating the local estimation condition number, we apply numerical observability analysis techniques to observations of satellites on trajectories in the Earth-Moon system, which has no general closed-form solution.

INTRODUCTION

Space domain awareness (SDA) and space traffic management (STM) are challenging due to an increasingly congested environment populated by a growing number of maneuverable vehicles and vehicles planned for deep space, i.e., beyond geosynchronous Earth orbit (GEO). Orbit design for the space-based cislunar domain awareness mission is an important topic due to the large range and limited viewing geometries between Earth-orbiting satellites and satellites in cislunar orbits. Complex astrodynamics must be modeled for objects in cislunar space, since lunar gravity cannot be neglected or treated as a perturbation to a dynamic model for cislunar object tracking, as it can in dynamic models of Earth-orbiting vehicles.

The cislunar regime is of increasing interest to the space industry due to its value for applications such as astronomy, interplanetary mission staging, lunar exploration and communications, and Earth orbit insertion.[1] Spacecraft placed in Earth-Moon collinear Lagrange points L1 and L2 avoid the gravity wells of the Earth and Moon, surface environmental issues, and artificial and natural space debris. These spacecraft require low station-keeping propellant (on the order of centimeters per second) and can travel with low propellant cost between L1 and L2 or between Earth-Moon space and Sun-Earth space.[2]

In July 2019, a near-rectilinear halo orbit (NRHO) about Earth-Moon L1 was chosen as the orbit for the future Lunar Gateway, which will be developed by the U.S.' National Aeronautics

[*]Graduate Student, Department of Aerospace Engineering, University of Maryland, 8197 Regents Drive, Room 1141, College Park, MD 20742, efowler3@umd.edu.

[†]Undergraduate Student, Department of Aerospace Engineering, University of Maryland, College Park, MD 20742, shurtt1@umd.edu.

[‡]Willis H. Young Jr. Professor of Aerospace Engineering Education, Department of Aerospace Engineering and Institute for Systems Research, University of Maryland College Park, 3150 Glenn L. Martin Hall, College Park, MD 20742, dpaley@umd.edu.

and Space Administration (NASA) and the European Space Agency (ESA) to serve as a solar-powered communications hub, science laboratory, short-term habitation module, and holding area for rovers and other robots.[1] Cislunar orbits can also be used as storage locations for spare Earth-orbiting satellites, allowing responsive insertion of these spares into operational Earth orbits with none of the indications and warnings normally associated with launch of a new vehicle into Earth orbit.[3] However, despite the desirable characteristics of certain cislunar orbits, NASA's ARTEMIS P1 (THEMIS B) and ARTEMIS P2 (THEMIS C) were the first two satellites to achieve orbit around an Earth-Moon Lagrange point in 2010.[4] As the opportunities offered by the cislunar regime become realities in the near future, space domain awareness and space traffic management specific to this environment will become increasingly critical capabilities. Preliminary results from this study could be used to inform the requirements for future cislunar space domain awareness systems, i.e., by placing satellites into specific orbits and constellations that maximize performance for SDA and STM missions.

Various models describe motion in the Earth-Moon system, including approaches using patched conics by switching among two-body models with the Earth, the Sun, and the Moon as central bodies; three-body models including the Earth and the Moon as primary masses; n-body models that directly incorporate the gravitational effects from more bodies than the two primaries; and models that incorporate perturbations like solar radiation pressure. A three-body model, which is used here, may be derived from a set of simplifying assumptions. The restricted three-body problem assumes that a body of negligible mass moves under the influence of two massive bodies. The circular restricted three-body problem additionally assumes that the two primary masses move in nearly circular orbits about their barycenter. For the Earth-Moon system, these assumptions are valid since a large spacecraft of 5900 kg would have less than 10^{-16} times the force on the primaries that the primaries would have on each other, and the Moon's orbit has an eccentricity of only 0.055.[5] The Circular Restricted Three-Body Problem (CR3BP) is used here as the basis for a dynamic simulation in which the relative motion of two or more satellites of negligible mass is studied.

In closely related prior work, Knister applied Model-Based Systems Engineering in order to assess the performance and financial burden of a given system of SDA sensors based on CR3BP dynamics.[6] Knister's metric Mean Detect Time (MDT), which is the ratio between the time during which the object of interest can be detected and the total time of the simulation, is the complement of one of our metrics (inavailability, described below). In order to evaluate whether or not an object can be detected, MDT incorporates a lower threshold for signal-to-noise ratio (SNR) based on illumination, whereas our comparable metric includes information on whether or not a target object is obscured by the Moon or Earth from the perspective of the observer or within a Sun exclusion angle from the perspective of the observer, without considering target object illumination. Additionally, Knister does not consider our range and angular interval metrics in his evaluation, and we do not consider tracking or cost metrics. Whereas we evaluate target objects in L1 and L2 halo orbits, L1 and L2 Lyapunov orbits, and L4 planar orbits, Knister only evaluates target objects in L1 Lyapunov orbits. Furthermore, we evaluate observers in these L1, L2, and L4 orbits, as well as Keplerian Earth and Moon orbits, whereas Knister evaluates observers in Earth orbits only (various LEO and GEO). Using the local estimation condition number, we are additionally able to analyze cases with multiple observers as well as single observers.

Our approach to studying space-based observability in the Earth-Moon system begins with the development of a catalog of trajectories representing a range of Earth and Moon orbits propagated

in the Earth-Moon system, Earth-Moon L1 and L2 Lyapunov orbits (closed trajectories that remain in the plane of the Earth-Moon system), Earth-Moon L1 and L2 halo orbits (closed trajectories that include an out-of-plane component with respect to the Earth-Moon system and are controlled to maintain matching in-plane and out-of-plane frequencies), and in-plane Earth-Moon L4 orbits. Using this catalog of trajectories in the Earth-Moon system, we make various pairings to represent observer and target trajectories, where an observer trajectory can be any trajectory in the catalog, and target trajectories are restricted to be Lagrange point orbits only (L1, L2, L4). By studying the evolution of the relative geometries of these pairings over time and adding one year of Sun ephemeris from the Jet Propulsion Laboratory (JPL) Horizons database, we are able to calculate several heuristic metrics of interest to space-based cislunar domain awareness missions.[7] For instance, we calculate how long it would take the target object to pass through an angular unit of the observer's field of view, how often the target object would be hidden behind the Earth or the Moon from the perspective of the observer, how often the observer may not be able to point an optical sensor at the target due to a Sun exclusion angle, and the range from the observer to the target, which could be used to determine (for instance) signal-to-noise ratio for an optical sensor given a specific target size and illumination.

After reviewing these heuristic metrics for space-based observability in the Earth-Moon system, we then apply a numerical observability analysis technique, which adds further understanding to pairings of one observer with one target and permits consideration of multiple observers in different trajectories observing a single target. Krener and Ide offer a method for calculating the empirical local observability gramian matrix based on the nominal initial state of the target trajectory, as well as perturbed versions of this initial state with their corresponding output.[8] The empirical local observability gramian is equivalent to the local observability gramian for sufficiently small perturbation.[8] We take the common logarithm of the condition number of this gramian and use it to compare observability for measurements of a target trajectory from chosen observer trajectories. A smaller condition number represents better observability (as do smaller values for all previously described heuristic metrics). We choose the measurement to be the vector from the observer to the target. Our first set of results includes average values for this metric across all observer trajectories in each family. That is, a result for the Earth-orbiting observer family is the average of this condition number for Earth-orbiting observer trajectories across a range of semi-major axes, eccentricities, and inclinations.

To consider observability when a two-observer constellation may observe a single target, we choose the measurement to be the vectors from each observer to the target. Our second set of results, for constellations of observers rather than single observers, includes only the condition number for this gramian based on the nominal observer trajectory from the orbit family in question rather than an average across all trajectories in the family. For example, the nominal Earth-orbiting trajectory has the nominal semi-major axis, eccentricity, and inclination as defined in our catalog of cislunar trajectories. Combining our heuristic metrics for single observers to extend our analysis to constellations of observers is not straightforward, so to analyze cases with multiple observers we use only the theoretically justified empirical observability metric, recognizing that this metric takes into account the dynamics of the system as well as its geometry.

The contributions of this paper are (1) evaluation of the estimation performance of cislunar orbits from an observing cislunar, lunar, or Earth orbit using nonlinear observability theory; (2) pairwise analysis of target and observer orbits spanning Keplerian and Lagrangian orbit families, comparing our nonlinear observability metric with heuristics like range, inavailability, and angular interval;

and (3) evaluation of the estimation performance of constellations of two observers against cislunar targets. Application of nonlinear observability theory to the cislunar space domain awareness problem shows that L2 halo target orbits are particularly difficult to observe from all observer orbit families. Although the range heuristic for L4 planar orbits reflects the large range between Lagrange point L4 and other parts of cislunar space, these orbits are shown to be both observable from other parts of cislunar space and high-performing as observers in both the single-observer case and the two-observer case with an L1 Lyapunov target. L1 and L2 observer orbits also provide an improvement in numerical observability for an L1 Lyapunov target when combined with an Earth orbiting observer. This analysis advances research in the fields of cislunar dynamics and observability so as to allow the selection of effective orbits for satellites that may be launched in the near future to accomplish the space-based cislunar domain awareness mission.

The outline of the paper is as follows. The next section provides background information on cislunar dynamics, including a description of the circular restricted three-body problem (CR3BP), calculations of the locations and stability characteristics of the five equilibrium (Lagrange) points in the CR3BP, a discussion of the types of periodic motions that can be found about Lagrange points in the Earth-Moon system, and an explanation of some of the challenges to cislunar space domain awareness. The following section describes the ways in which we have quantified the observability of cislunar trajectories using heuristic and theoretically justified metrics from numerical observability. Next, we provide results representing how various observer-target trajectory pairings fare against our heuristic and observability metrics. Finally, we provide results representing how constellations of two observers perform using the empirical observability metric given a target in an L1 Lyapunov trajectory.

CISLUNAR DYNAMICS

The Circular Restricted Three-Body Problem

Motion within the Earth-Moon system may be approximated using the dynamics of the Circular Restricted Three-Body Problem (CR3BP), in which the motion of a spacecraft with negligible mass is modeled under the influence of the gravitation of two primaries approximated as point masses.[9] By convention, the motion of the spacecraft is described using a coordinate system that rotates with the rate of rotation of the Earth and Moon in circular orbits about their barycenter. The planar CR3BP has two degrees of freedom, whereas the spatial CR3BP has three. Only one constant of motion exists, known as the Jacobi integral.

Since $\mathbf{r}_{CM} = \frac{m_1\mathbf{r}_1+m_2\mathbf{r}_2}{m_1+m_2} = \mathbf{0}$, $r_1 = \frac{-m_2 r_2}{m_1} = \frac{-m_2}{m_1}(r_{12}+r_1)$, where $r_{12} = r_1 + r_2$ is the constant distance between the two primaries m_1 and m_2, then $r_2 = \frac{m_1}{m_1+m_2}r_{12}$. The free-body diagram for m_2 shown in Fig. 1 gives $\frac{Gm_1m_2}{r_{12}^2} = m_2 r_2\omega^2 = \frac{m_1m_2}{m_1+m_2}r_{12}\omega^2$, which implies that the system shown in Fig. 2 rotates at a rate of[10]

$$\omega = \sqrt{\frac{G(m_1+m_2)}{r_{12}^3}}. \tag{1}$$

The free-body diagram for the spacecraft m in Fig. 1 provides the basis for the equations of motion in the CR3BP. The inertial acceleration is $\mathbf{a}_i = \mathbf{a}_0 + \mathbf{a}_m + 2\boldsymbol{\omega}\times\mathbf{v} + \dot{\boldsymbol{\omega}}\times\mathbf{r} + \boldsymbol{\omega}\times(\boldsymbol{\omega}\times\mathbf{r})$, where $\mathbf{a}_0$ is the translational acceleration of the rotating frame, $\mathbf{a}_m$ is the acceleration of the spacecraft in the rotating frame, $2\boldsymbol{\omega}\times\mathbf{v}$ is the Coriolis acceleration, $\dot{\boldsymbol{\omega}}$ is the time derivative of $\boldsymbol{\omega}$ with respect to

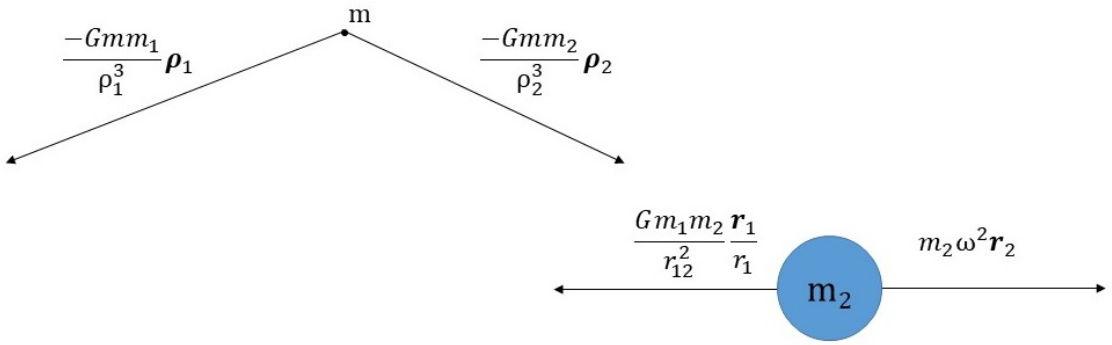

Figure 1. Free-body diagrams of spacecraft m (left) and smaller primary mass m_2 (right).

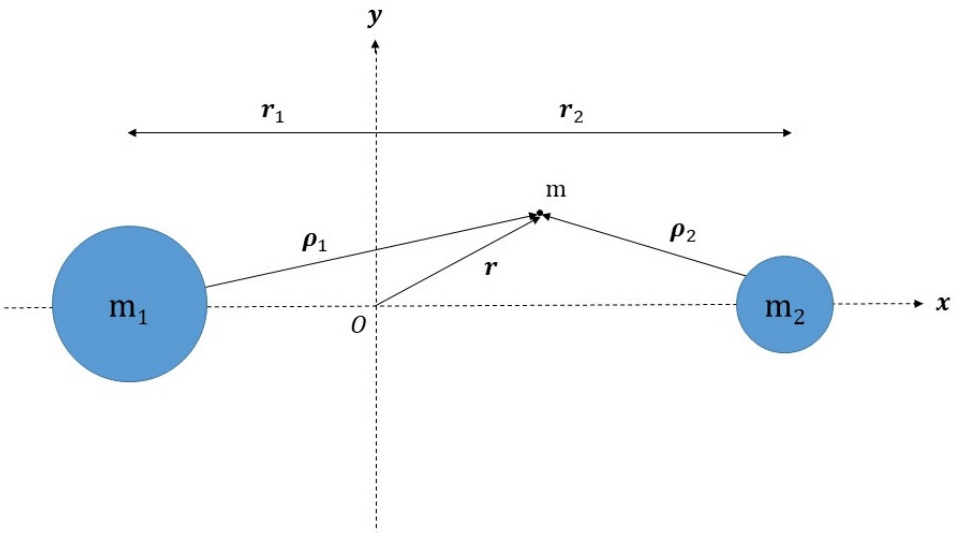

Figure 2. Circular Restricted Three-Body Problem. Mass m is a spacecraft of negligible mass compared to $m_1 \geq m_2$, which are two large primary masses.

the rotating frame, and $\boldsymbol{\omega} \times (\boldsymbol{\omega} \times \mathbf{r})$ is the centripetal acceleration. Because $\mathbf{a}_0 = \mathbf{0}, \dot{\boldsymbol{\omega}} \times \mathbf{r} = \mathbf{0}$, and $\mathbf{a}_m = \ddot{\mathbf{r}}$, we have

$$\ddot{\mathbf{r}} = \mathbf{a}_i - 2\boldsymbol{\omega} \times \mathbf{v} - \boldsymbol{\omega} \times (\boldsymbol{\omega} \times \mathbf{r}). \tag{2}$$

Newton's second law gives $\mathbf{a}_i = -G[\frac{m_1}{\rho_1^3}\rho_1 - \frac{m_2}{\rho_2^3}\rho_2]$, with $\rho_1 = \mathbf{r} - \mathbf{r}_1$ $= \begin{bmatrix} x - \frac{-m_2 r_{12}}{m_1+m_2} & y & z \end{bmatrix}^T$ and $\rho_2 = \mathbf{r} - \mathbf{r}_2 = \begin{bmatrix} x - \frac{m_1 r_{12}}{m_1+m_2} & y & z \end{bmatrix}^T$. The CR3BP rotates about the z axis in the frame shown in Fig. 2 (by convention in the $+z$ direction), giving $\boldsymbol{\omega} = \begin{bmatrix} 0 & 0 & \omega \end{bmatrix}^T$.

Therefore Eq. 2 becomes

$$\ddot{\mathbf{r}} = \frac{-Gm_1}{||\mathbf{r}-\mathbf{r}_1||}\begin{bmatrix} x+\frac{m_2}{m_1+m_2}r_{12} \\ y \\ z \end{bmatrix} - \frac{Gm_2}{||\mathbf{r}-\mathbf{r}_2||}\begin{bmatrix} x-\frac{m_1}{m_1+m_2}r_{12} \\ y \\ z \end{bmatrix} + 2\omega\begin{bmatrix} \dot{y} \\ -\dot{x} \\ 0 \end{bmatrix} + \omega^2\begin{bmatrix} x \\ y \\ 0 \end{bmatrix}. \quad (3)$$

By convention, position, velocity, and mass are nondimensionalized in the CR3BP, so that the distance between the Earth and the Moon (r_{12}) becomes unity, as are the mean motion of the two primaries and the universal gravitational constant G.[10] The Earth's mass is denoted $1-\mu$ and the Moon's mass is μ. One distance unit is defined as $1DU \equiv r_{12}$, one mass unit as $1MU \equiv m_1+m_2$ (so that mass ratio is $\mu = \frac{m_2}{m_1+m_2}$), and one time unit as $1TU \equiv \frac{T}{2\pi}$, where the orbital period T of the primaries about their barycenter is $T = \frac{2\pi}{\omega} = 2\pi\sqrt{\frac{r_{12}^3}{G(m_1+m_2)}}$ (a sidereal month).[11]

Using this nondimensionalization, the equations of motion for a spacecraft of negligible mass m from Eq. 3 become[11]

$$\begin{bmatrix} \ddot{x} \\ \ddot{y} \\ \ddot{z} \end{bmatrix} = -\frac{(1-\mu)}{\rho_1^3}\begin{bmatrix} x+\mu \\ y \\ z \end{bmatrix} - \frac{\mu}{\rho_2^3}\begin{bmatrix} x-1+\mu \\ y \\ z \end{bmatrix} + \begin{bmatrix} 2\dot{y} \\ -2\dot{x} \\ 0 \end{bmatrix} + \begin{bmatrix} x \\ y \\ 0 \end{bmatrix}. \quad (4)$$

Table 1. Constants used for nondimensionalizing the Earth-Moon system

Unit	Variable	Value
Earth-Moon system orbital period	T	27.3215 days
Time unit	TU	4.348 days
Distance unit	DU	384400 km
Speed unit	SU	1.023 km/s
Mass ratio	μ	0.012277471

By convention, a state in the system with a positive ($+z$) angular momentum (such that the spacecraft is moving counter-clockwise in the Earth-Moon rotating frame) is considered prograde, whereas a clockwise motion is considered retrograde.[12] A solution in the CR3BP can be one of four types:[13] an equilibrium point, a periodic orbit (Lyapunov or halo), a quasi-periodic orbit (Lissajous), and chaotic motion.

Equilibrium Points in the CR3BP

At equilibrium points in the CR3BP (known as Lagrange or libration points), gravitational forces and rotational accelerations are balanced.[11] At stable equilibrium points, perturbations cause oscillations about the equilibrium point, whereas at unstable equilibrium points, perturbations cause drift away from the equilibrium point. Collinear Lagrange points L1, L2, and L3 are saddle points; there is a family of periodic orbits surrounding each of these points: the planar periodic orbits called Lyapunov orbits and their three-dimensional counterparts called halo and Lissajous orbits.[9] The z-axis solution to the linear part of Eq. 3, obtained by setting $x=0$ and $y=0$, is simple harmonic. Linearized analysis of the coupled xy behavior of Eq. 3 further reveals two real roots of opposite sign and two imaginary roots. Since the two real roots are opposite in sign, arbitrarily chosen initial conditions give rise to unbounded solutions as time increases, but if initial conditions are restricted

such that only the non-divergent mode is allowed, the coupled motion in the xy plane is bounded and periodic.[9]

To derive the locations of these equilibrium points, we note that equilibrium points occur where the gradient of the pseudopotential U vanishes, where

$$U = \frac{1}{2}\omega^2(x^2 + y^2) + \frac{1-\mu}{\rho_1} + \frac{\mu}{\rho_2}. \tag{5}$$

Note that

$$\begin{bmatrix} \ddot{x} \\ \ddot{y} \\ \ddot{z} \end{bmatrix} = \begin{bmatrix} 2\omega\dot{y} + \frac{\partial U}{\partial x} \\ -2\omega\dot{x} + \frac{\partial U}{\partial y} \\ \frac{\partial U}{\partial z} \end{bmatrix}. \tag{6}$$

When a spacecraft is at rest at an equilibrium point, $\dot{x} = \ddot{x} = \dot{y} = \ddot{y} = \dot{z} = \ddot{z} = 0$, which implies $\frac{\partial U}{\partial x} = \frac{\partial U}{\partial y} = \frac{\partial U}{\partial z} = 0$. Since $\frac{\partial U}{\partial z} = -z\mu((x-1+\mu)^2 + y^2 + z^2)^{-\frac{3}{2}}$, then $z = 0$ is the only solution of $\frac{\partial U}{\partial z} = 0$, meaning that all Lagrange points lie in the xy plane of the rotating frame defined in Fig. 2.[10]

Using U in terms of μ, ρ_1, and ρ_2, trivial solutions to $\frac{\partial U}{\partial x} = \frac{\partial U}{\partial \rho_1}\frac{\partial \rho_1}{\partial x} + \frac{\partial U}{\partial \rho_2}\frac{\partial \rho_2}{\partial x} = 0$ and $\frac{\partial U}{\partial y} = \frac{\partial U}{\partial \rho_1}\frac{\partial \rho_1}{\partial y} + \frac{\partial U}{\partial \rho_2}\frac{\partial \rho_2}{\partial y} = 0$ may be found. When $\frac{\partial U}{\partial \rho_1} = (1-\mu)(\rho_1 - \frac{1}{\rho_1^2})$ and $\frac{\partial U}{\partial \rho_2} = \mu(\rho_2 - \frac{1}{\rho_2^2})$ are set to 0, $\rho_1 = \rho_2 = 1$, meaning that the distances from the primaries to the spacecraft are the same and also equal to the distance between the primaries, forming an equilateral triangle. These points are known as L4 and L5.[10]

Stating $x^2 + y^2$ in terms of μ, ρ_1, and ρ_2, Eq. 5 becomes

$$U = (1-\mu)(\frac{\rho_1^2}{2} + \frac{1}{\rho_1}) + \mu(\frac{\rho_2^2}{2} + \frac{1}{\rho_2}) - \frac{\mu(1-\mu)}{2}. \tag{7}$$

To define the locations of the remaining equilibrium points (L1, L2, and L3), full solutions for $\frac{\partial U}{\partial x}$ and $\frac{\partial U}{\partial y}$ (and thus for $\frac{\partial \rho_1}{\partial x}$, $\frac{\partial \rho_1}{\partial y}$, $\frac{\partial \rho_2}{\partial x}$, $\frac{\partial \rho_2}{\partial y}$) are required. Given $\frac{\partial \rho_1}{\partial y} = \frac{y}{\rho_1}$ and $\frac{\partial \rho_2}{\partial y} = \frac{y}{\rho_2}$, the solution $\frac{\partial U}{\partial y} = (1-\mu)(\rho_1 - \frac{1}{\rho_1^2})(\frac{y}{\rho_1}) + \mu(\rho_2 - \frac{1}{\rho_2^2})(\frac{y}{\rho_2}) = 0$ reveals that $y = 0$ for the remaining equilibrium points L1, L2, and L3, described as the collinear Lagrange points because they lie on the line drawn between the Earth and the Moon (the x axis in the CR3BP synodic frame). Given $\frac{\partial \rho_1}{\partial x} = \frac{x+\mu}{\rho_1}$ and $\frac{\partial \rho_2}{\partial x} = \frac{x-1+\mu}{\rho_2}$, the positions of L1, L2, and L3 along the x axis are found from the solution $\frac{\partial U}{\partial x} = (1-\mu)(\rho_1 - \frac{1}{\rho_1^2})(\frac{x+\mu}{\rho_1}) + \mu(\rho_2 - \frac{1}{\rho_2^2})(\frac{x-1+\mu}{\rho_2}) = 0$, i.e.,

$$\begin{aligned} x_{L1} &= (1-\mu) - \rho_2 \\ x_{L2} &= \rho_2 + (1-\mu) \\ x_{L3} &= -\rho_1 - \mu. \end{aligned} \tag{8}$$

The solutions to Eq. 8 are found numerically as functions of mass ratio μ.[13] See Fig. 3 for a depiction of the geometry of the Lagrange points.

Cislunar Orbits

Lyapunov orbits and halo orbits are periodic motions about the collinear Earth-Moon Lagrange points (L1, L2, L3). Lyapunov orbits lie entirely in the plane of the two primary bodies (the xy plane

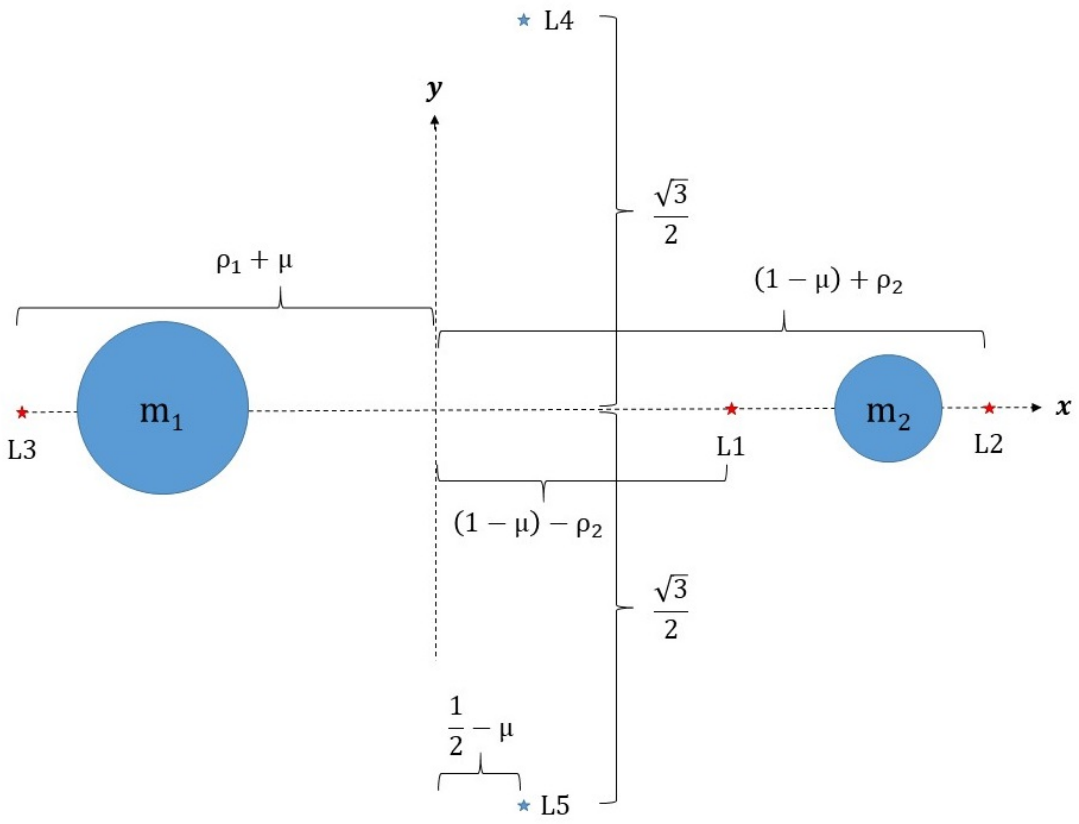

Figure 3. Locations of Lagrange points for the CR3BP. L4 and L5 are stable equilibrium points, whereas L1, L2, and L3 are saddle points.

shown in Fig. 2), whereas halo orbits include an out-of-plane component. L1 Lyapunov orbits, L2 Lyapunov orbits, and L4 planar orbits considered in this analysis are shown in Fig. 4. Halo orbits considered in this analysis are shown in Fig. 5. Orbits about the Earth-Moon L2 point are called halo orbits when the size of the orbit is comparable to the distance to L2 from the Moon, resulting in periodic three-dimensional motion, and when controlled such that the frequency of the out-of-plane motion matches that of the in-plane motion. An L2 halo orbit requires relatively low ΔV to reach from Earth, and with sufficiently large amplitude it allows continuous Earth visibility, appearing as an elliptical motion around the Moon from the perspective of the Earth .[12]

Challenges for Cislunar Space Domain Awareness

Objects in cislunar orbits are approximately ten times farther from the Earth's surface than objects being tracked in geostationary or geosynchronous earth orbits (GEO/GSO).[14] Given current technology, optical systems based on the Earth's surface are capable of detecting only very large objects (hundreds of meters in size) at those distances. Deep-space missions for science and exploration have used cooperative methods for orbit determination (e.g., two-way Doppler tracking) at these and larger ranges, but for space domain awareness and space traffic management purposes, cooperative methods cannot be assumed.[15] Additionally, objects in cislunar space appear to move very slowly from the perspective of an observer based on the Earth's surface or even orbiting the

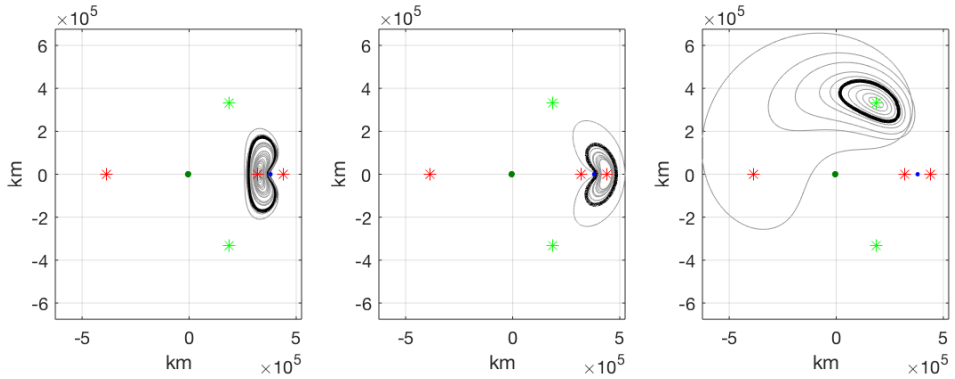

Figure 4. Visualizations in the Earth-Moon plane of (from left to right) the L1 and L2 Lyapunov and L4 planar orbits described in Table 2 with the nominal orbits in bold. The Earth and Moon are shown to scale in the appropriate locations. The range of orbit periods shown for L1 orbits is 13.1-28.6 days, for L2 orbits 14.8-31.1 days, and for L4 orbits 27.5-28.7 days.

Earth, such that there may be insufficient geometric diversity in the observations for the observer to detect motion and create an orbit estimate, whether a detection is defined as a streak across a focal plane or a time-stamped series of collections against an unresolved point. Objects in the cislunar environment can also spend significant time in front of or behind the Moon or the Earth, or within a Sun- or Moon-exclusion angle with respect to an observer's sensor, which could cause an observer to lose custody of the object. These considerations form the basis for the metrics proposed in the section on heuristic observability metrics below.

QUANTIFYING THE OBSERVABILITY OF CISLUNAR ORBITS

Observability Gramian

To investigate the cislunar space domain awareness and orbit determination problem in cases when it is of interest to find a degree of observability rather than a binary result describing only whether or not a phenomenon is observable, a numerical method is used.[8] The observability gramian measures the sensitivity of a chosen measurement or output to the initial conditions of the system. The local observability gramian is defined as

$$P(x^0) = \int_0^T \Phi'(t)H'(t)H(t)\Phi(t)dt \tag{9}$$

where Φ is the fundamental matrix solution of the linear dynamics and H is the measurement Jacobian. This gramian can be expensive to compute because it requires computation of Φ and H, and linearization can lose important insights into a nonlinear system. Krener and Ide offer a method for calculating the (i, j) components of the $n \times n$ empirical local observability gramian matrix $P(\mathbf{x}^0)$:

$$\frac{1}{4\epsilon^2}\int_0^T (\mathbf{y}^{+i}(t) - \mathbf{y}^{-i}(t))'(\mathbf{y}^{+j}(t) - \mathbf{y}^{-j}(t))dt \tag{10}$$

where $\mathbf{x}^0$ is the nominal initial state of the target trajectory, $\mathbf{x}^{\pm i} = \mathbf{x}^0 \pm \epsilon\mathbf{e}^i$ and $\mathbf{y}^{\pm i}(t)$ are the perturbed state and corresponding output, $\epsilon > 0$ is a small displacement, and $\mathbf{e}^i$ is the ith unit vector

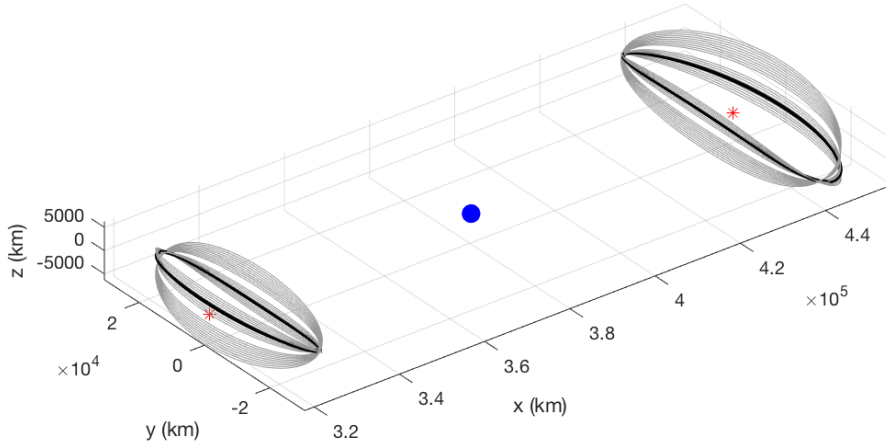

Figure 5. Visualization of the range of L1 and L2 halo orbits described in Table 2, with the nominal orbits in bold. Class I halos tilt in the $-x$ direction toward the Earth (not pictured), whereas Class II halos tilt in the $+x$ direction. The Moon is shown to scale in the appropriate location. The L1 halo orbit period is ~ 12.5 days, and the L2 halo orbit period is ~ 14.7 days.

in $\mathbb{R}^n$.[8] The condition number for the resulting matrix is the ratio of the largest local singular value to the smallest; a large condition number indicates that the estimation problem is ill-conditioned for the given states, whereas smaller condition number equates to better observability.[16] If the observed dynamical system is smooth, meaning that all partial derivatives exist and are continuous, then this gramian converges to the local observability gramian for $\epsilon \to 0$.[8] The empirical gramian requires only the ability to simulate the observed dynamical system rather than a solution to the dynamics.[8]

In order to acquire an empirical observability metric result, we start by loading an observer trajectory from our catalog and defining initial conditions $\mathbf{x}_{0,tar}$ for the 6×1 target state. Additionally, we define a time step t_{step} and a small perturbation ϵ. We then define 12 perturbed initial condition vectors $\mathbf{x}_{0+i}$ and $\mathbf{x}_{0-i}$, $i = 1, \ldots, 6$, which represent initial conditions perturbed in the positive and negative directions by ϵ in the position components and by $\frac{2\pi\epsilon}{T}$ in the velocity components (so that perturbation ϵ has a properly scaled effect on velocity as compared to its effect on position). We propagate these initial conditions using CR3BP dynamics in Eq. 4. We can then find measurements $\mathbf{y}$ from the observer trajectory to the trajectories resulting from the 12 perturbed initial condition vectors for the target. We calculate $\mathbf{y}$ at each time step as a 4×1 vector composed of the 3×1 unit vector direction to the target from the observer concatenated with the scalar range between target and observer. Finally, we use Eq. 10 with a Riemann sum approximation of the integral over our finite time steps to calculate the components of the 6×6 empirical local observability gramian. We use Matlab's `cond` function to find the condition number of the gramian, and we take the common logarithm of this condition number to find our final empirical observability metric as shown in Fig. 7.

Heuristic Observability Metrics

In order to use a CR3BP dynamic simulation to analyze various orbit pairings, we additionally define several heuristic observability metrics. Since an estimate of the trajectory of an object is

based on observations, the object must have some apparent motion with respect to the observer.[17] For instance, if the target sits in the same pixel of an observer's optical sensor for the entire period of time while the observer waits for the development of a streak indicating motion, building a track on this observation will be difficult to impossible. Our first metric is the inverse of the relative angular rate, defined as time per degree of motion of the observed object from the perspective of the observer. A lower value for this metric represents a more observable orbit. This metric is calculated by first taking the azimuth and elevation of the target object from the observer, with respect to the Earth-Moon synodic frame. Azimuth is calculated as the anticlockwise angle between the $+x$ axis and the projection of the vector from the observer to the target onto the xy plane. Elevation is the angle between the $+x$ axis and the projection of the vector from the observer to the target onto the xz plane. The angle of interest is the angle through which the target passes from the perspective of the observer in a single simulation time step, calculated as $d\theta = \sqrt{dAz^2 + dEl^2}$ using the small angle approximation. We take the average value of $\frac{d\theta}{dt}$, with simulation time step one hour, over the entire simulation time (one year), and the inverse of this average is the metric result that appears in Fig. 7.

Other viewing geometry concerns, like occultation by the Earth or Moon and Sun exclusion angles for optical sensors, reduce the amount of time that an object of interest is viewable by the observer. Therefore, the second metric is the percentage of the simulation time during which the target object is unavailable to the observer for any of these reasons. A lower value for this metric represents a more observable orbit. Earth and Moon positions and sizes are directly available in the CR3BP simulation, and we add the Sun's position by assuming a mission start date of January 1, 2010 and using downloaded Sun ephemeris data with respect to the Earth-Moon barycenter from the JPL Horizons database (https://ssd.jpl.nasa.gov/horizons.cgi). Fig. 6 depicts the Moon in its various phases and the way that the Sun-Earth-Moon geometry evolves over time with these phases. The same figure also depicts the types of inavailability that we have considered in our analysis, including obscuration of a target by the Earth and the Moon (represented by a depiction of obscuration of a target by the Moon on the left side of the figure) and placement of a target within a 30^o sun exclusion angle (depicted on the right side of the figure).

Finally, we consider the range between the observer and the object being observed. Target range affects different sensors in different ways. Signal-to-noise ratio for an optical sensor decreases as the square of the range; received power for radar decreases as the fourth power of the range. However, regardless of sensor phenomenology, large range will negatively affect performance for a cislunar SDA mission. Since objects in orbit around or near the Moon are approximately ten times farther from Earth than the farthest objects being tracked in other space domain awareness efforts (i.e., objects in GEO), range is a critical third metric that can be reduced by prudent placement of space-based assets.

While metrics from numerical observability are theoretically justified and thus the emphasis of ongoing work, supplementing early analysis with heuristic metrics has allowed for a more intuitive understanding of the cislunar system. Additionally, the inavailability metric is not implicitly incorporated into the numerical observability metric in the same way as range and angular interval, so a consideration of inavailabilities should be integrated into the numerical observability metric calculation in order to ensure that this information is not lost in future investigations using only the numerical observability metric.

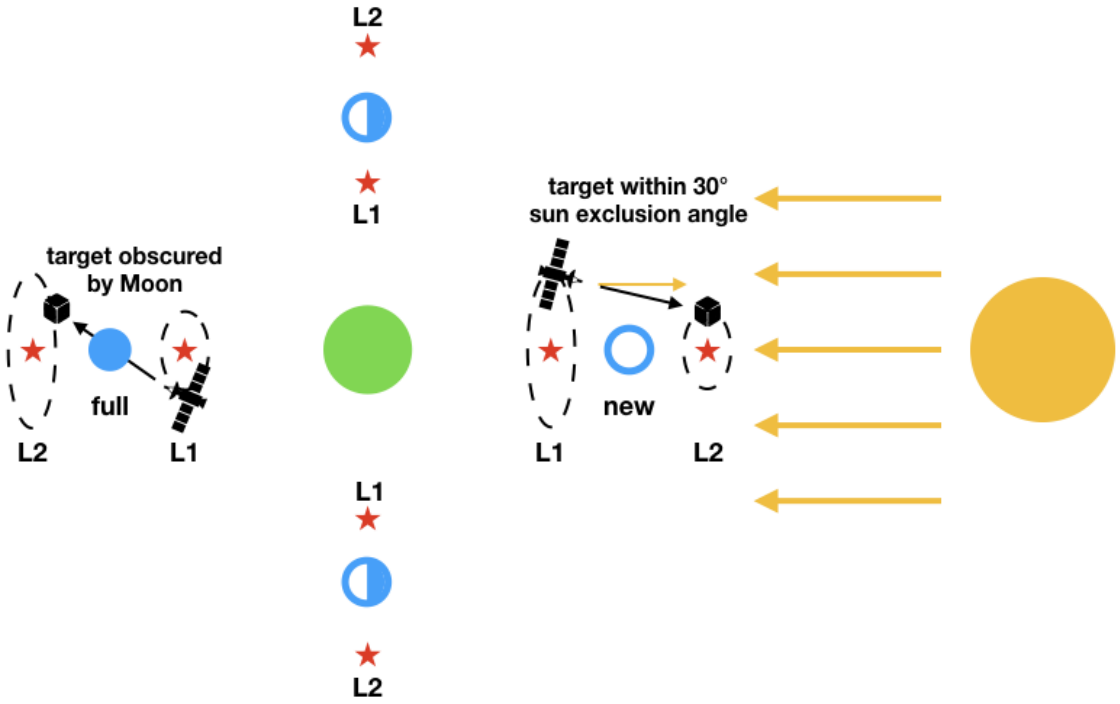

Figure 6. Depiction of Sun-Earth-Moon geometry during different Moon phases. Additionally, on the left is an illustration of inavailability due to obscuration of a target by the Moon from an observer's perspective, and on the right is an illustration of inavailability due to a target's placement within a 30^o sun exclusion angle for an optical sensor. This depiction is simplified since the Sun is actually not quite in the same plane as the Earth-Moon system, which is inclined by 5.145^o with respect to the ecliptic plane.

PERFORMANCE EVALUATION OF CISLUNAR OBSERVING ORBITS

Table 2 shows the orbit families considered in this analysis, as well as their variable parameters. The target objects in this analysis were placed in trajectories according to the nominal value of each parameter for the given family, and the observer orbits were varied across the range of values for each parameter. The nominal orbits (using nominal values in Table 2) are shown in bold in the previous visualizations of these orbits (Fig. 4, 5). Lyapunov orbits about L1 and L2 were generated according to Broucke.[18] Halo orbits about L1 and L2 were generated according to Richardson.[19] A class I halo is defined by Richardson to be a halo where the $+z$ up part of the halo tilts toward $-x$, and a class II halo is defined by Richardson to be a halo where the $+z$ up part of the halo tilts toward $+x$. Periodic trajectories about L4 were generated according to Grebow.[20] We used a one-hour time step in all cases. Trajectories were integrated over a year, which is a sufficiently long period of time to produce a generalized result, independent of epoch. The geometry of the Moon, Earth, and Sun evolves over time, exhibiting periodic behavior over a lunar synodic month (29.5 days), but the lunar orbital plane is inclined with respect to the ecliptic plane by 5.145^o. Thus, without accounting for precession, it takes one year to observe all possible relative geometries.[6]

Table 2. Orbit families and their defining parameters. *Non-dim* indicates that length is given in non-dimensionalized units (divided by the average distance between the Earth and the Moon). Position components x, y, and z for the Lagrange point orbits are given in the Earth-Moon rotating frame.

Orbit Family	Variable Parameters	Parameter Range	Nominal Value
Keplerian Earth	semi-major axis a	$8378 - 42378$ (km)	25378
	eccentricity e	$0 - 0.5$ (unitless)	0.05
	inclination i	$0 - 90$ (deg)	45
Keplerian Moon	semi-major axis a	$1837 - 2937$ (km)	2387
	eccentricity e	$0 - 0.25$ (unitless)	0.05
	inclination i	$0 - 90$ (deg)	45
L1 Lyapunov	initial state (position component x)	$0.643 - 0.809$ (non-dim)	0.711
L2 Lyapunov	initial state (position component x)	$1.178 - 1.359$ (non-dim)	1.253
L1 Halo	amplitude in z	$1000 - 5500$ (km)	3000
	class	I or II (unitless)	1
L2 Halo	amplitude in z	$1000 - 5500$ (km)	3000
	class	I or II (unitless)	1
L4 Planar	initial state (position component x)	$0.475 - 0.979$ (non-dim)	0.727

Figure 7 summarizes the observability results for pairings of observer orbits and target orbits. Range and angular interval are expected to follow a trend similar to that of the empirical observability metric since range and direction are incorporated in the measurement vector definition for the empirical observability calculation. Inavailability is not included in the empirical observability metric (which for instance includes no information about the position of the Sun and so cannot include solar exclusion angle considerations), so it is not expected to follow the same trend as the empirical observability metric.

Numerical observability provides consistent results within each target orbit family, with L4 planar target orbits proving the most observable at $13.8 - 14.1$ and L2 halo target orbits proving the most difficult to observe at $19.9 - 20.4$. L2 halo observer orbits and L1 Lyapunov observer orbits provide the best observations of L4 planar targets according to numerical observability, despite their mediocre to poor performance in the heuristic metrics. An L2 halo provides the best observations of another L2 halo according to numerical observability, and this result matches predictably good results for range and angular interval when an L2 halo observer is tasked to collect observations of an L2 halo target.

From our analysis we cannot definitively derive consistent trends to connect the numerical observability metric to the heuristic metrics. The heuristic metrics which consider only geometry do not take into account the underlying dynamics of the system which are considered in the observability metric. The observability metric acknowledges the chaotic nature of the CR3BP for most initial conditions by allowing us to measure the extent to which small perturbations to the initial conditions of a given trajectory create changes that appear in the available measurements, supporting its use in further examinations in the next section.

PERFORMANCE EVALUATION OF CONSTELLATIONS OF CISLUNAR OBSERVERS

Whereas combining our heuristic metrics for single observers to extend our analysis to constellations of observers is not straightforward, we are able to calculate the empirical observability metric for more than one observer using the same process as defined above except that we load two observer trajectories from our catalog and define measurement $\mathbf{y}$ at each time step as an 8×1 vector concatenation of the following quantities: the 3×1 unit vector direction to the target from the first observer, the scalar range between the target and first observer, the 3×1 unit vector direction to the

Observer orbit family	Target orbit family: L1 halo		L2 halo		L1 Lyapunov		L2 Lyapunov		L4 planar	
Keplerian Earth	86%	3%	117%	4%	96%	3%	108%	3%	102%	1%
	20%	18.5	21%	20.4	14%	17.7	13%	16.4	14%	13.9
Keplerian Moon	15%	2%	17%	2%	35%	1%	28%	1%	107%	11%
	23%	18.8	24%	20.1	18%	17.6	14%	16.7	17%	13.9
L1 halo	1%	2%	31%	19%	34%	16%	33%	28%	101%	37%
	0%	18.5	21%	20.2	16%	17.6	14%	16.8	12%	13.9
L2 halo	31%	19%	1%	2%	42%	34%	30%	14%	117%	54%
	15%	18.9	2%	19.9	17%	17.5	9%	16.7	11%	13.8
L1 Lyapunov	28%	14%	39%	30%	41%	1%	46%	19%	102%	27%
	10%	18.4	16%	20.1	13%	17.4	14%	16.8	18%	13.8
L2 Lyapunov	34%	22%	27%	13%	51%	27%	35%	16%	115%	51%
	13%	18.9	13%	20.0	14%	17.7	18%	16.6	11%	14.1
L4 planar orbit	139%	2%	159%	5%	141%	2%	155%	4%	77%	1%
	14%	18.8	15%	20.1	13%	17.2	16%	16.9	14%	13.9

Key:	worst quartile	range (% avg Earth-Moon distance)	angular interval (% day)
	middle quartiles	inavailability (% simulation time)	empirical observability
	best quartile		

Figure 7. Performance for observer-target pairings against the proposed metrics. Lower values represent better observer performance against a given target orbit family for all metrics.

target from the second observer, and the scalar range between the target and second observer. The process may thus also be scaled to observer constellations with more than two spacecraft in future work.

Figure 8 summarizes the observability results for pairings of observer orbits against an L1 Lyapunov target orbit. These results are shown as the percent improvement in empirical observability, as compared to a single nominal observer from family 1, that can be obtained when an observer from family 2 is added to the constellation. L4 planar orbits provide by far the most improvement in observability when combined with an observer in any other orbit considered here. L1 and L2 observer orbits also provide a distinct improvement when combined with an Earth orbiting observer. Two observers provide generally better observability than one due to the additional geometric diversity that a second observer provides, supplementing the measurement vector in the empirical observability calculation so that it has a higher likelihood of being affected by small perturbations in the initial conditions of the target.

CONCLUSION

The viability of Keplerian and cislunar orbit families for cislunar space domain awareness has been evaluated using heuristic metrics and an empirical observability metric. Application of nonlinear observability theory to the cislunar space domain awareness problem has shown that L2 halo

	Observer orbit family 2						
	Keplerian Earth	Keplerian Moon	L1 halo	L2 halo	L1 Lyapunov	L2 Lyapunov	L4 planar
Observer orbit family 1							
Keplerian Earth	0.6%	8.3%	12.1%	15.4%	23.3%	20.8%	64.4%
Keplerian Moon		7.3%	2.9%	8.8%	17.4%	6.2%	54.6%
L1 halo				5.7%	13.1%	3.6%	49.2%
L2 halo					10.9%		50.6%
L1 Lyapunov		1.3%	1.2%	13.7%	8.2%	12.8%	53.6%
L2 Lyapunov				2.7%	14.2%	1.1%	56.7%
L4 planar orbit							

Key:	worst quartile
	middle quartiles
	best quartile

Figure 8. Empirical observability results for constellations of two observers against an L1 Lyapunov target orbit, shown as the percent improvement over the result for the single nominal observer orbit from family 1 when the nominal observer orbit from family 2 is added to the constellation. Family nominal values from Table 2 are used to define these observer orbits. Gray entries indicate that no improvement was measured.

target orbits are particularly difficult to observe from all observer orbit families. Although the range heuristic for L4 planar orbits reflects the large range between L4 and other parts of cislunar space, these orbits are shown to be both observable from other parts of cislunar space and high-performing as observers in both the single-observer case and the two-observer case with an L1 Lyapunov target. L1 and L2 observer orbits also provide an improvement in numerical observability for an L1 Lyapunov target when combined with an Earth orbiting observer. Future work includes extending the empirical observability results to include constellations of three or more observers from various of the orbit families described here, discarding measurements that coincide with periods of target inavailability from the empirical observability calculation, and finally considering the ΔV required for station-keeping in these orbits in order to further evaluate the viability of these orbits for cislunar SDA missions.

ACKNOWLEDGMENT

E. Fowler is supported by the U.S. Naval Research Laboratory Edison Memorial Graduate Training Program.

REFERENCES

[1] S. Lizy-Destrez, L. Beauregard, E. Blazquez, S. Manglativi, and V. Quet, "Rendezvous Strategies in the Vicinity of Earth-Moon Lagrangian Points," *Frontiers in Astronomy and Space Sciences*, Vol. 5, 2019, pp. 1–19, 10.3389/fspas.2018.00045.

[2] M. R. Bobskill and M. L. Lupisella, "The Role of Cis-Lunar Space in Future Global Space Exploration," *Proceedings of the Global Space Exploration Conference*, Washington, District of Columbia, 2012, pp. 1–15. May 22–24, 2012. Paper number GLEX-2012.05.5.4x12270.

[3] J. Chase, N. Chow, E. Gralla, and N. J. Kasdin, "LEO Constellation design using the lunar L1 point," *Proceedings of the 14th AAS/AIAA Space Flight Mechanics Meeting*, Maui, HI, 2004, pp. 1–19. February 8–12, 2004. Paper number AAS 04-248.

[4] T. A. Pavlak and K. C. Howell, "Evolution of the Out-of-Plane Amplitude for Quasi-Periodic Trajectories in the Earth-Moon System," *Acta Astronautica*, Vol. 81, No. 2, 2012, pp. 456–465.

[5] B. L. Jones, *A Guidance and Navigation System For Two Spacecraft Rendezvous in Translunar Halo Orbit*. PhD thesis, University of Texas at Austin, Austin, TX 78712, 5 1993.

[6] S. R. Knister, "Evaluation Framework for Cislunar Space Domain Awareness (SDA) Systems," Master's thesis, Air Force Institute of Technology, Wright-Patterson Air Force Base, Ohio, 2020. 3243. AFIT-ENV-MS-20-M-221.

[7] R. S. Park and A. B. Chamberlin, "Jet Propulsion Laboratory Horizons Database," `https://ssd.jpl.nasa.gov/horizons.cgi`.

[8] A. J. Krener and K. Ide, "Measures of Unobservability," *Proceedings of the 48th IEEE Conference on Decision and Control (CDC) held jointly with the 2009 28th Chinese Control Conference*, Shanghai, China, 2009, pp. 6401–6406.

[9] W. S. Koon, M. W. Lo, J. E. Marsden, and S. D. Ross, *Dynamical Systems, the Three-Body Problem and Space Mission Design*. Springer, 2007.

[10] J. M. A. Danby, *Fundamentals of Celestial Mechanics*. Willmann-Bell, 2nd ed., 1992.

[11] A. E. Roy, *Orbital Motion*. Taylor & Francis Group, 4th ed., 2005.

[12] J. S. Parker and R. L. Anderson, *Low-Energy Lunar Trajectory Design*. Wiley, 1st ed., 6 2014.

[13] G. Gomez, J. Llibre, R. Martinez, and C. Simo, *Dynamics and Mission Design Near Libration Points, Fundamentals: The Case of Collinear Libration Points*, Vol. 2 of *World Scientific Monograph Series in Mathematics*. World Scientific Publishing, 4 2001.

[14] R. R. Bate, D. D. Mueller, and J. E. White, *Fundamentals of Astrodynamics*. Dover, 1971.

[15] M. Beckman, "Orbit Determination Issues for Libration Point Orbits," *Proceedings of the International Conference of Libration Point Orbits and Applications*, Girona, Spain, 2002, pp. 1–9. June 10–14, 2002. Paper number 20020081023.

[16] E. Kaufman, T. A. Lovell, and T. Lee, "Nonlinear Observability for Relative Orbit Determination with Angles-Only Measurements," *Journal of Astronautical Sciences*, Vol. 63, 2016, pp. 60–80. 10.1007/s40295-015-0082-9.

[17] D. A. Vallado, *Fundamentals of Astrodynamics and Applications*. Microcosm Press and Kluwer Academic Publishers, 2nd ed., 2001.

[18] R. A. Broucke, "Periodic Orbits in the Restricted Three-Body Problem with Earth-Moon Masses," Tech. Rep. 321168, Jet Propulsion Laboratory, Pasadena, CA, February 1968.

[19] D. L. Richardson, "Analytic Construction of Periodic Orbits about the Collinear Points," *Celestial Mechanics*, Vol. 22, 1980, pp. 241–253.

[20] D. J. Grebow, "Generating Periodic Orbits in the Circular Restricted Three-Body Problem with Applications to Lunar South Pole Coverage," Master's thesis, Purdue University, West Lafayette, IN, May 2006.